



Large-field-of-view optical resolution photoacoustic microscopy

WEI QIN,^{1,2,3} TIAN JIN,^{1,2,3} HENG GUO,^{1,2} AND LEI XI^{1,2,*}

¹Department of Biomedical Engineering, Southern University of Science and Technology, Shenzhen, Guangdong, 518055, China

²School of Physical Electronics, University of Electronic Science and Technology of China, Chengdu, 610054, China

³These authors contributed equally to this work

*xilei@sustc.edu.cn

Abstract: The use of existing optical resolution photoacoustic microscopy (ORPAM) has been limited to small organs or part of large organs due to the millimeter-scale field of view (FOV) in both lateral and axial directions. Here, we report a large-field-of-view ORPAM (L-ORPAM) using a combination of a new scanning mechanism and an ultrafast pulsed laser. Phantom and *in vivo* experiments show that L-ORPAM has a spatial FOV of 40 mm in lateral and 12 mm in axial, which expands the effective imaging domain to one order that of existing ORPAMs. To show the advantages of L-ORPAM, we apply it to imaging vasculatures of both brain and ears simultaneously in mice, and to visualizing intestinal vasculatures in rats. The result suggests that L-ORPAM has sufficient contrast, resolution and spatial FOV to carry out studies of large rodents.

© 2018 Optical Society of America under the terms of the [OSA Open Access Publishing Agreement](#)

OCIS codes: (110.0180) Microscopy; (110.5120) Photoacoustic imaging; (170.6900) Three-dimensional microscopy.

References and links

1. P. Beard, "Biomedical photoacoustic imaging," *Interface Focus* **1**(4), 602–631 (2011).
2. V. Ntziachristos, "Going deeper than microscopy: the optical imaging frontier in biology," *Nat. Methods* **7**(8), 603–614 (2010).
3. J. Yao, L. Wang, J. M. Yang, K. I. Maslov, T. T. W. Wong, L. Li, C. H. Huang, J. Zou, and L. V. Wang, "High-speed label-free functional photoacoustic microscopy of mouse brain in action," *Nat. Methods* **12**(5), 407–410 (2015).
4. L. V. Wang and S. Hu, "Photoacoustic tomography: *in vivo* imaging from organelles to organs," *Science* **335**(6075), 1458–1462 (2012).
5. Y. He, L. Wang, J. Shi, J. Yao, L. Li, R. Zhang, C.-H. Huang, J. Zou, and L. V. Wang, "*In vivo* label-free photoacoustic flow cytography and on-the-spot laser killing of single circulating melanoma cells," *Sci. Rep.* **6**(1), 39616 (2016).
6. S. Hu, K. Maslov, and L. V. Wang, "Second-generation optical-resolution photoacoustic microscopy with improved sensitivity and speed," *Opt. Lett.* **36**(7), 1134–1136 (2011).
7. H. Wang, X. Yang, Y. Liu, B. Jiang, and Q. Luo, "Reflection-mode optical-resolution photoacoustic microscopy based on a reflective objective," *Opt. Express* **21**(20), 24210–24218 (2013).
8. W. Song, W. Zheng, R. Liu, R. Lin, H. Huang, X. Gong, S. Yang, R. Zhang, and L. Song, "Reflection-mode *in vivo* photoacoustic microscopy with subwavelength lateral resolution," *Biomed. Opt. Express* **5**(12), 4235–4241 (2014).
9. Z. Chen, S. Yang, and D. Xing, "Optically integrated trimodality imaging system: combined all-optical photoacoustic microscopy, optical coherence tomography, and fluorescence imaging," *Opt. Lett.* **41**(7), 1636–1639 (2016).
10. L. Lin, P. Zhang, S. Xu, J. Shi, L. Li, J. Yao, L. Wang, J. Zou, and L. V. Wang, "Handheld optical-resolution photoacoustic microscopy," *J. Biomed. Opt.* **22**(4), 041002 (2016).
11. J. Y. Kim, C. Lee, K. Park, G. Lim, and C. Kim, "Fast optical-resolution photoacoustic microscopy using a 2-axis water-proofing MEMS scanner," *Sci. Rep.* **5**(1), 7932 (2015).
12. Y. Yuan, S. Yang, and D. Xing, "Optical-resolution photoacoustic microscopy based on two-dimensional scanning galvanometer," *Appl. Phys. Lett.* **100**(2), 023702 (2012).
13. H. Kang, S. W. Lee, E. S. Lee, S. H. Kim, and T. G. Lee, "Real-time GPU-accelerated processing and volumetric display for wide-field laser-scanning optical-resolution photoacoustic microscopy," *Biomed. Opt. Express* **6**(12), 4650–4660 (2015).
14. L. Li, C. Yeh, S. Hu, L. Wang, B. T. Soetikno, R. Chen, Q. Zhou, K. K. Shung, K. I. Maslov, and L. V. Wang, "Fully motorized optical-resolution photoacoustic microscopy," *Opt. Lett.* **39**(7), 2117–2120 (2014).

15. B. Rao, L. Li, K. Maslov, and L. Wang, "Hybrid-scanning optical-resolution photoacoustic microscopy for *in vivo* vasculature imaging," *Opt. Lett.* **35**(10), 1521–1523 (2010).
16. W. Qi, T. Jin, J. Rong, H. Jiang, and L. Xi, "Inverted multiscale optical resolution photoacoustic microscopy," *J. Biophotonics* **10**(12), 1580–1585 (2017).
17. T. Jin, H. Guo, H. Jiang, B. Ke, and L. Xi, "Portable optical resolution photoacoustic microscopy (pORPAM) for human oral imaging," *Opt. Lett.* **42**(21), 4434–4437 (2017).
18. T. Jin, H. Guo, L. Yao, H. Xie, H. Jiang, and L. Xi, "Portable optical-resolution photoacoustic microscopy for volumetric imaging of multiscale organisms," *J. Biophotonics* e201700250 (2017).
19. H. Guo, C. Song, H. Xie, and L. Xi, "Photoacoustic endomicroscopy based on a MEMS scanning mirror," *Opt. Lett.* **42**(22), 4615–4618 (2017).
20. L. V. Wang and J. Yao, "A practical guide to photoacoustic tomography in the life sciences," *Nat. Methods* **13**(8), 627–638 (2016).
21. C. Zhang, K. Maslov, J. Yao, and L. V. Wang, "*In vivo* photoacoustic microscopy with 7.6- μm axial resolution using a commercial 125-MHz ultrasonic transducer," *J. Biomed. Opt.* **17**(11), 116016 (2012).
22. L. Zhu, L. Li, L. Gao, and L. V. Wang, "Multi-view optical resolution photoacoustic microscopy," *Optica* **1**(4), 217–222 (2014).

Introduction

Optical resolution photoacoustic microscopy (ORPAM), integrating the merits of rich optical contrast, high spatial resolution and deep acoustic penetration in a single modality, remains one of the fastest evolving optical imaging techniques in the last decade and has been extensively applied in biology and medicine [1–5]. Conventional ORPAMs, utilizing mechanical raster scanning mechanisms, suffers from low imaging speed, small field of view (FOV), and translation of imaging interfaces/samples [6–9]. Limited by the moving speed of mechanical scanners, it is challenging for conventional ORPAMs to achieve a large lateral FOV. In addition, the use of objectives restricts the effective axial FOV to be ~ 1 mm. Although recent progress in ultrafast lasers and new acoustic/optical scanning mechanisms/devices promotes the development of ORPAM [10–15], it is still challenging to extend the FOV. Furthermore, the translation of imaging interfaces/samples is not convenient to image large-size organs/rodents. Our recent study demonstrates the use of a rotary scanning mechanism enabling translationless of both imaging interface and samples [16–18]. However, the spatial FOV is not large enough to image large organs, especially organs with curved surfaces. In this letter, we report a large-field-of-view ORPAM (L-ORPAM) using the combination of a new optical/acoustic scanning mechanism and an ultrafast pulsed laser, which enables translationless between the imaging interface and samples. L-ORPAM has an ultra-wide lateral and axial FOVs of 40 mm and 12 mm, respectively. To show the ultra-wide imaging capability of L-ORPAM, we image the mouse brain and ears simultaneously, and visualize the intestinal vasculatures of rats.

Methods

2.1 System configuration

Figures 1(a) and 1(b) present the schematic of the system and the volumetric layout of the imaging interface. Laser pulses, conveyed from a 532 nm pulsed laser (GLPM-10, IPG Photonics) with a maximal repetition rate of 600 kHz and a duration of ~ 7 nanoseconds (ns), are coupled into a single mode fiber (460HP, Nuferr) via a customized space-to-fiber coupler consisting of two convex lenses, a 15 μm pinhole, an objective lens (GCO-2112, Daheng Optics), and a multidimensional manipulator. Partial energy is reflected into a fast photodiode to record the fluctuation of laser pulses. A two-dimensional (2D) galvanometer scanner (GVS012/M, Thorlabs), equipped with an F-Theta scan lens (FTH100-1064, Thorlabs), which has a maximal imaging domain of 70 mm \times 70 mm and a working distance of 107 mm, is mounted on a three-dimensional manual stage to optimize the position of optical focal plane. The scanner is driven by a multifunctional data acquisition card (PCI-6731, National Instrument). A motorized rotator (RAP-125, Zolix) is used to rotate the transducers in a high speed. The ultrathin cover glass tilted with an angle of 45° allows the transmission of the light to the sample, and the reflection of the light-induced sound to a special customized cylindrically

focused transducer (Olympus IMS) which has a focal length of 63.5 mm, a center frequency of 10 MHz, an aperture of 25.4 mm, and a bandwidth of 71%. The PA signals are amplified by ~39dB using an amplifier (5073PR, Olympus IMS) and digitized by a high-speed data acquisition card (ATS-9325, Alazar Inc.).

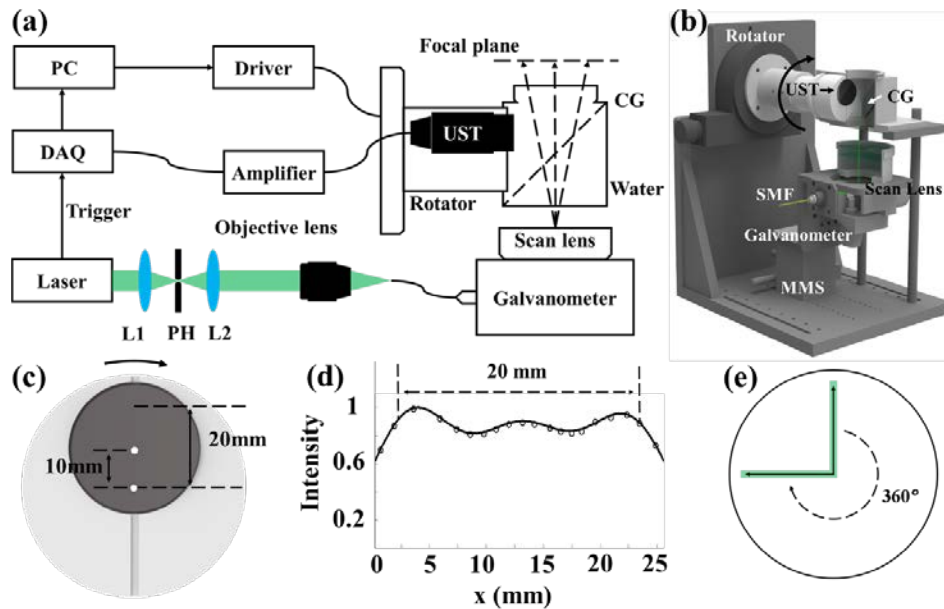


Fig. 1. The schematic and scanning mechanism of L-ORPAM. (a) Illustration of system configuration. PC: personal computer, DAQ: data acquisition card, L1: lens 1, L2: lens 2, PH: pinhole, CG: cover glass, UST: ultrasound transducer. (b) The layout of the imaging interface. SMF: single mode fiber, CG: cover glass, MMS: manual multidimensional stage, UST: ultrasound transducer. (c) Close-up view of the acoustic detection unit. (d) Profile of sensitivity distribution in the acoustic focal zone of the cylindrically focused ultrasound transducer. (e) Illustration of the scanning mechanism. Black arrows: optical scan line, green bar: acoustic focal zone, dotted arrow: rotational scanning trace of the optical scan line and acoustic focal zone. The animation in [Visualization 1](#) depicts the scanning mechanism of optical focus and acoustic focal zone.

Figure 1(c) presents the close-up view of the detection unit. To avoid the use of marginal area of the focal zone, the transducer center is positioned 10 mm away from the rotational center. The sensitivity distribution of the transducer is profiled in Fig. 1(d), in which there is a flat-response area with a length of 20 mm in the focal zone. To obtain the best signal to noise ratio (SNR), the acoustic focal zone (green bar in Fig. 1(d)) is overlapped with the optical scan line (black arrows in Fig. 1(e)). [Visualization 1](#) shows an animation depicting the scanning mechanism. The acoustic focal zone keeps stationary and the optical focus scans in line (black arrows in Fig. 1(e)). Afterwards, both acoustic focal zone and optical scan line rotates with a given step angle (the dashed black arrow in Fig. 1(e)) until the FOV is fully covered. No translation of the sample or the imaging interface is required and one volume is acquired with a 360° angular rotation of both optical scan line and acoustic focal zone. For all the experiments except specially specified cases, we collected 2000 depth-resolved photoacoustic signals, termed as A-lines, in one cross-sectional image (B-scan) and 10000 B-scans to form a volumetric image.

In term of imaging speed, it is primarily limited by the laser repetition rate and the maximal scanning speed of the galvanometer scanner. The experimental time theoretically equals to the number of scanning points divided by the maximal laser repetition rate, which is 34 seconds in current experimental setup. However, the maximal scanning speed of the scanner driven by the

function of saw-tooth is up to 50 Hz, which limits the number of B-scans (up to 50) per second. Therefore, a volume for phantom and *in vivo* experiments with 10000 B-scans would cost ~200 seconds using the laser repetition rate of 100 kHz. It is feasible to promote the imaging speed by using faster optical scanners [19,20].

2.2 Phantom preparation

The grid phantom has a transparent background, a size of 70 mm in diameter and contains ten 0.7 mm pencil leads which are aligned in two perpendicular directions with an interval of 10 mm. The carbon fiber phantom with a given optical absorption coefficient of 0.07 mm⁻¹ and a reduced scattering coefficient of 1 mm⁻¹ has a size of 50 mm in diameter and consists of numerous carbon fibers on the top surface to simulate the vascular networks in biological tissues. The suture line phantom consisting of several black suture lines has a transparent background and dimensions of 40 mm × 18 mm. A sharp blade is placed on the flat surface of a transparent phantom with a diameter of 60 mm to measure the distribution of lateral resolution in the focal plane. To evaluate the distribution of lateral resolution in depth, a sharp blade is inserted into a transparent phantom with a diameter of 60 mm and tilted with an angle.

2.3 Animals preparation

BALB/c Mice and Male Wistar rats were freely laid down on a heating pad to maintain the body temperature at 37°C. The ears and brains of the mice were gently depilated to avoid strong photoacoustic signals from hairs, and the scalps were carefully removed. Mice were anesthetized using a nose mask with continual flow of a mixture of isoflurane and air. Rats were anaesthetized with chloral hydrate (50mg/kg) by intraperitoneal injection. The abdomens of rats were incised using a surgical blade to expose the intestine. After the experiments, all mice and rats were sacrificed using a standard procedure approved by the University of Electronic Science and Electronic of China (UESTC).

2.4 Data processing and imaging reconstruction

We used Matlab 2014a to derive the envelopes of A-lines using Hilbert transform, directly back-project A-lines to reconstruct a B-scan image, stack all the B-scans following their rotational traces in a polar coordinate to rebuild a volumetric image, and project the maximum value of each A-line in axial direction to form a maximum amplitude projection (MAP) image. We produced movies using MATLAB 2014a and Amira 5.3.3.

Due to the inhomogeneous spatial sampling pattern induced by the scanning mechanism, we calculated a map of weighting factors based on the number of scans in each pixel. The original value of each pixel in the polar coordinate was divided by the corresponding weight factor to remove the non-uniformity of the reconstructed images. In addition, the uneven detection sensitivity of the transducer would lead to unbalanced photoacoustic intensity in B-scans. We used the sensitivity distribution of the transducer in the focal zone to calibrate each B-scan. Furthermore, each A-line was divided by the photon energy measured by the fast photodiode to remove the fluctuation of laser pulses.

Results and discussion

3.1 System characterization

We evaluated the lateral FOV of L-ORPAM using a grid phantom (Fig. 2(a)). Figure 2(b) presents the MAP image of the phantom, in which there is no distortion over the entire imaging area and the maximal lateral FOV is measured as 40 mm. Figures 2(c) and 2(d) present the MAP image and the B-scan along the dashed orange line of the phantom. We can clearly identify all embedded suture lines in both MAP image and B-scan, and observe stronger PA signals in the focal plane (the yellow dashed line in Fig. 2(d)). The maximal axial FOV is estimated to be 12 mm by calculating the distance between the top and bottom suture lines in

B-scan. [Visualization 2](#) shows the sequential MAP images projected from different depths. The results in Figs. 2(f) and 2(g) suggest that the lateral resolution deteriorates in the off-center and off-focal-plane areas. Therefore, we further evaluated the distribution of lateral resolution over the entire FOV using a sharp blade. We carried out the blade experiments using a finer frame size, in which there were 4000 A-lines in one B-scan and 20000 B-scans in one volume.

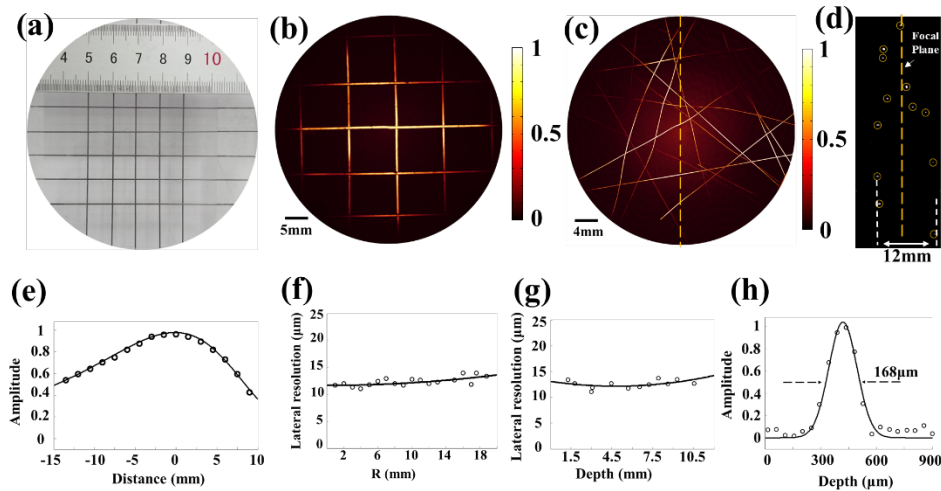


Fig. 2. Evaluation of system performance. (a) Photograph of the grid phantom used to estimate the lateral FOV of L-ORPAM. (b) Maximum amplitude projection (MAP) image of the grid phantom. (c) MAP image of a suture line phantom used to estimate the axial FOV of L-ORPAM. [Visualization 2](#) shows sequential MAP images projected from different depths. (d) A selected cross-sectional image consist of two B-scans with an angle of 180 degrees of the suture line phantom as indicated by the dashed yellow line in c. The yellow dashed line indicates the position of the imaging plane. (e) Axial sensitivity of the transducer. (f) Distribution of lateral resolution as the function of radius of FOV. (g) Distribution of lateral resolution in different depths. (h) A Gaussian-fitted profile of a typical A-line used to estimate the axial resolution of L-ORPAM.

We adjusted the optical focal plane to the phantom surface and carried out L-ORPAM imaging. We obtain the distribution of lateral resolution in the focal plane by measuring the full width at half maxima (FWHM) of the line spread function (LSF) derived from edge spread function (ESF) of the imaged blade edge in different locations over the entire FOV. As plotted in Fig. 2(f), the resolution in the center of the optical focal plane is $\sim 11.2 \mu\text{m}$ and becomes slightly worse in the off-center area. The resolution at the edge of the optical focal plane is $14.6 \mu\text{m}$, which represents the worst scenario. Based on the estimations using the imaged edges of the tilted blade, the lateral resolution is measured as $11.2 \mu\text{m}$ in the center of the imaging plane which is $\sim 6 \text{ mm}$ below the phantom surface (Fig. 2(g)). In the off-focal-plane areas, the lateral resolution becomes slightly worse and the worst one is measured as $14.8 \mu\text{m}$. The pulse energy at the optical focus is $\sim 120 \text{ nJ}$, leading to a variable photon energy ranged from 72 mJ/cm^2 to 122 mJ/cm^2 in water depending on the size of the optical focus. Due to the high optical scattering property of biological tissues, the photon density in the optical focal plane is much lower than the American National Standards Institute (ANSI) safety limit of 22 mJ/cm^2 . Figure 2(h) presents the Gaussian-fitted profile of a Hilbert-transformed A-line. The axial resolution is estimated to be $168 \mu\text{m}$ by measuring the FWHM of the profile, which is consistent with the theoretical value of $165 \mu\text{m}$ [21]. It is feasible to improve the axial resolution by using a high frequency transducer. However, it is quite difficult to fabricate a high-frequency transducer with an ultra-large active area. An alternative way is to employ a linear high-frequency transducer array that combines the merits of large active area and high center frequency. While, the use of an array would require a multi-channel amplifier and data acquisition system, and

thus will significantly increase the cost. In addition, it is possible to use a multi-view scanning to improve the axial resolution of ORPAM [22].

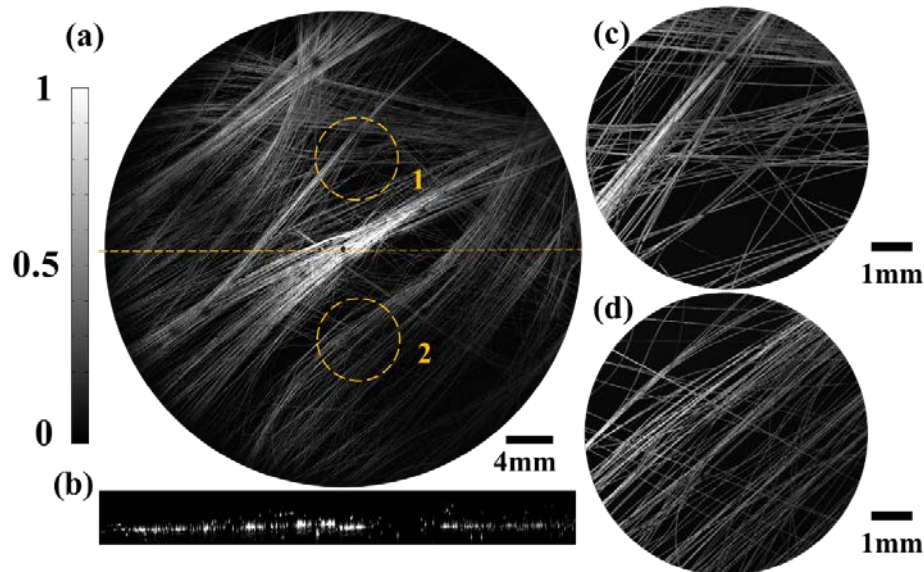


Fig. 3. L-ORPAM image of a carbon fiber phantom. (a) MAP image of the carbon fiber phantom with a frame size of 4000×4000 points in lateral FOV. (b) A selected cross-sectional image consist of two B-scans with an angle of 180 degrees along the dashed yellow line in (a), the scale bar is the same as (a). (c) and (d), Close-up views of sub regions indicated by two dashed yellow circles in (a). Figure 3(c) shows the enlarged view of region 1 and (d) presents the enlarged view of region 2. Visualization 3 shows the enlarged views of the MAP image in different locations.

3.2 Phantom experiments

Before *in vivo* experiments, we conducted L-ORPAM imaging of carbon fiber phantoms. Figures 3(a) and 3(b) present the MAP image and cross-sectional image along the dashed orange line of a typical carbon fiber phantom with numerous carbon fibers distributed on the top surface. We observe an ultra-dense carbon fiber network over the entire FOV, which has a frame size of 4000×4000 points. As shown in Figs. 3(c) and 3(d), the geometries of carbon fibers are well identified in two enlarged regions. Visualization 3 presents the close-up views of the full-view MAP image in different locations.

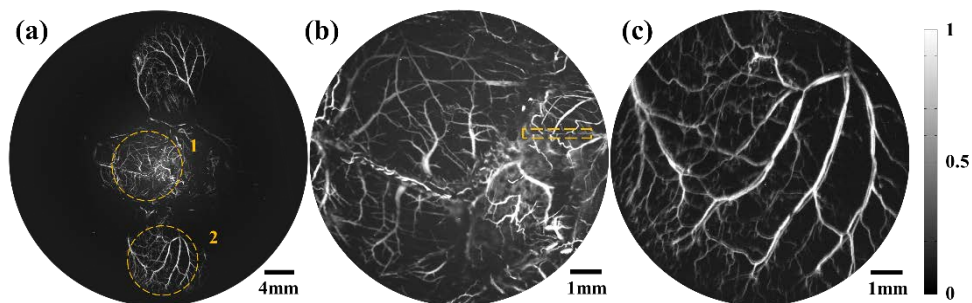


Fig. 4. *In vivo* L-ORPAM imaging of a mouse brain and two ears simultaneously. (a) MAP image of the brain and ears with an effective image domain of $\phi 40 \text{ mm} \times 6 \text{ mm}$. (b) and (c) Close-up views of two selected regions in the mouse brain (region 1) and ear (region 2) as indicated by two dashed yellow circles in (a). Visualization 4 displays MAP images projected from different depths for both entire and selected FOVs.

3.3 Animal experiments

To show the large-scale imaging capability of L-ORPAM, we carried out *in vivo* imaging of the mouse brain and ears simultaneously, and the intestinal vasculatures in the abdominal cavities of rats. Figure 4(a) presents the L-ORPAM MAP image of the brain and ears of a typical BALB/c mouse, which demonstrates the ultra-large-scale imaging capability of L-ORPAM for *in vivo* experiments. Figures 4(b) and 4(c) show two sub-regions in the brain (region 1) and ear (region 2), respectively. We clearly see the ultra-dense vascular networks in brain and ears with comparable contrast and resolution to conventional ORPAMs. The blood vessels in the area highlighted by a dashed orange box in Fig. 4(b) are partially discontinued due to the motion artifacts induced by breath. [Visualization 4](#) presents the sequential MAP images by projecting the volume data from different depths for the entire and selected FOVs. The maximal axial FOV in this case is 6 mm which could be fully covered by the effective FOV of L-ORPAM.

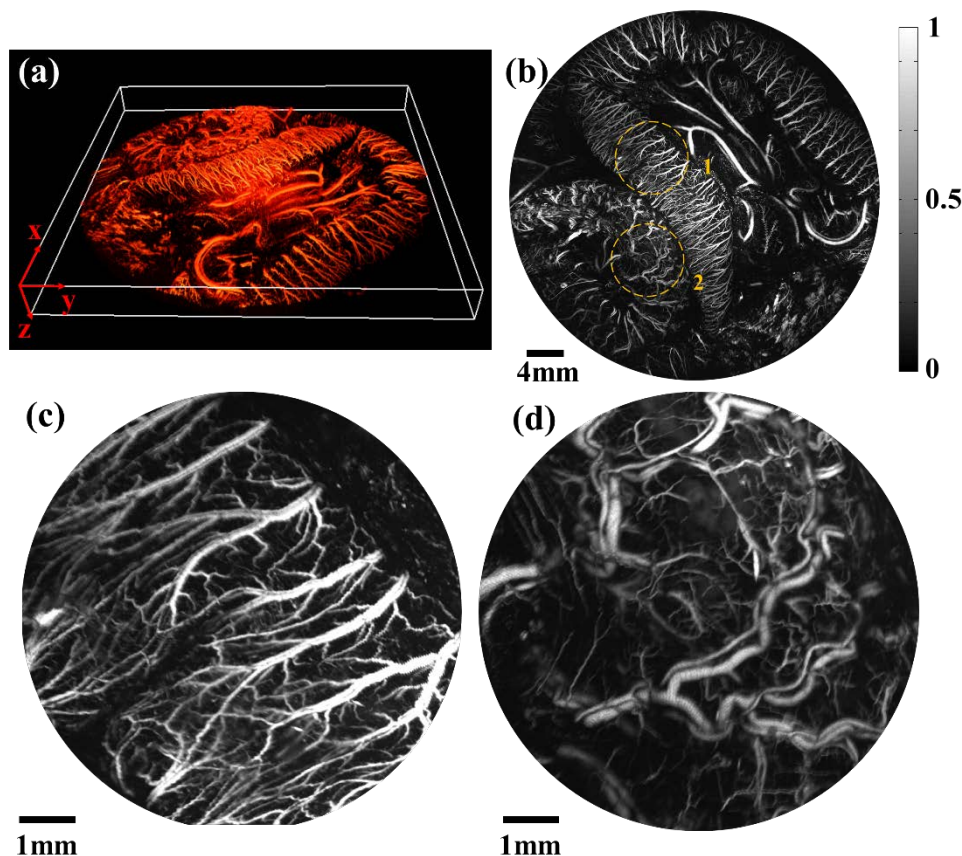


Fig. 5. *In vivo* L-ORPAM experiments of intestine in a rat abdomen. (a) Volume rendering of the intestine. The size is $40\text{mm} \times 40\text{mm} \times 4.5\text{mm}$. (b) MAP image of the intestine fulfilling the entire FOV. (c) and (d) Close-up views of two typical regions in Fig. 5(b). Figure 5(c) shows the enlarged view of region 1 and Fig. 5(d) illustrate the enlarged view of region 2. [Visualization 5](#) shows the volume rendering of the intestine in different views and sequential MAP images projected from different depths.

In addition to classic samples, we further carried out experiments to visualize vasculatures of intestine in rats, which could fulfill the entire FOV. Figures 5(a) and 5(b) illustrate the volumetric rendering and MAP image of the intestine, respectively. The FOV fulfilled by intestines has a denser vascular network in the central area than that of the marginal areas due

to the imbalanced resolving capability and imaging sensitivity of L-ORPAM. Figures 5(c) and 5(d) show the enlarged MAP images of two sub regions in Fig. 5(b). We observe two scenarios including the flat intestine without food (region 1 and Fig. 5(c)) and inflated intestine with food (region 2 and Fig. 5(d)). The vascular network in Fig. 5(c) is much denser than that of Fig. 5(d), while there are more capillaries in Fig. 5(d). In flat intestine, we can visualize a denser vascular network consisting blood vessels from both sides. In inflated intestine, although the light is unable to penetrate the feces, the intestine wall becomes thinner, making more capillaries visible to L-ORPAM. [Visualization 5](#) presents both volumetric structure of intestine in different views and sequential MAP images projected from different depths. Limited by the available animal models in our lab, we are only able to demonstrate the large-scale imaging capability of L-ORPAM using multiple organs and the organ system of small animals. However, the result suggests that L-ORPAM is the most promising ORPAM technique capable of visualizing vasculatures in major organs of large rodents with sufficient resolution, contrast and FOV.

Conclusions

In summary, we report the design and evaluation of a large-field-of-view ORPAM, which enables translationless of both imaging interface/samples, and provides a lateral FOV of 40 mm and an axial FOV of 12 mm with a high lateral resolution of up to 11.2 μm and a moderate axial resolution of 168 μm . *In vivo* studies reveal the advantages of L-ORPAM over all the existing ORPAMs and demonstrate the feasibility of applying it for studying large animals.

Funding

National Natural Science Foundation of China (61775028, 81571722, 61528401); Southern University of Science and Technology (start-up grant); State International Collaboration Program from Sichuan (2016HH0019).